

Low-Energy Effective Hamiltonian for Giant-Gap Quantum Spin Hall Insulators in Honeycomb X-Hydride/Halide ($X = \text{N-Bi}$) Monolayers

Cheng-Cheng Liu,¹ Shan Guan,¹ Zhigang Song,² Shengyuan A. Yang,³ Jinbo Yang,^{2,4} and Yugui Yao^{1,*}

¹*School of Physics, Beijing Institute of Technology, Beijing 100081, China*

²*State Key Laboratory for Mesoscopic Physics, and School of Physics, Peking University, Beijing 100871, China*

³*Engineering Product Development, Singapore University of Technology and Design, Singapore 138682, Singapore*

⁴*Collaborative Innovation Center of Quantum Matter, Beijing, China*

Using the tight-binding method in combination with first-principles calculations, we systematically derive a low-energy effective Hilbert subspace and Hamiltonian with spin-orbit coupling for two-dimensional hydrogenated and halogenated group-V monolayers. These materials are proposed to be giant-gap quantum spin Hall insulators with record huge bulk band gaps opened by the spin-orbit coupling at the Dirac points, e.g., from 0.74 to 1.08 eV in BiX ($X = \text{H, F, Cl, and Br}$) monolayers. We find that the low-energy Hilbert subspace mainly consists of p_x and p_y orbitals from the group-V elements, and the giant first-order effective intrinsic spin-orbit coupling is from the on-site spin-orbit interaction. These features are quite distinct from those of group-IV monolayers such as graphene and silicene. There, the relevant orbital is p_z and the effective intrinsic spin-orbit coupling is from the next-nearest-neighbor spin-orbit interaction processes. These systems represent the first real 2D honeycomb lattice materials in which the low-energy physics is associated with p_x and p_y orbitals. A spinful lattice Hamiltonian with an on-site spin-orbit coupling term is also derived, which could facilitate further investigations of these intriguing topological materials.

PACS numbers: 73.43.-f, 73.22.-f, 71.70.Ej, 85.75.-d

I. INTRODUCTION

Recent years have witnessed great interest in two-dimensional (2D) layered materials with honeycomb lattice structures. Especially, the 2D group-IV honeycomb lattice materials, such as successively fabricated graphene,^{1,2} and silicene,^{3,4} have attracted considerable attention both theoretically and experimentally due to their low-energy Dirac fermion behavior and promising applications in electronics. Recently, we have discovered stable 2D hydrogenated and halogenated group-V honeycomb lattices via first-principles (FP) calculations.⁵ Their structures are similar to that of a hydrogenated silicene (silicane), as shown in Fig. 1(a). In the absence of spin-orbit coupling (SOC), the band structures show linear energy crossing at the Fermi level around K and K' points of the hexagonal Brillouin zone. It is quite unusual that the low-energy bands of these materials are of p_x and p_y orbital character. Previous studies in the context of cold atoms systems have shown that p_x and p_y orbital character could lead to various charge and orbital ordered states as well as topological effects.^{6,7} Our proposed materials, being the first real condensed matter systems in which the low-energy physics is associated with p_x and p_y orbitals, are therefore expected to exhibit rich and interesting physical phenomena.

The quantum spin Hall (QSH) insulator state has generated great interest in condensed matter physics and material science due to its scientific importance as a novel quantum state and its potential technological applications ranging from spintronics to topological quantum computation.⁸⁻¹⁰ This novel electronic state is gaped in the bulk and conducts charge and spin in gapless edge states without dissipation protected by time-reversal

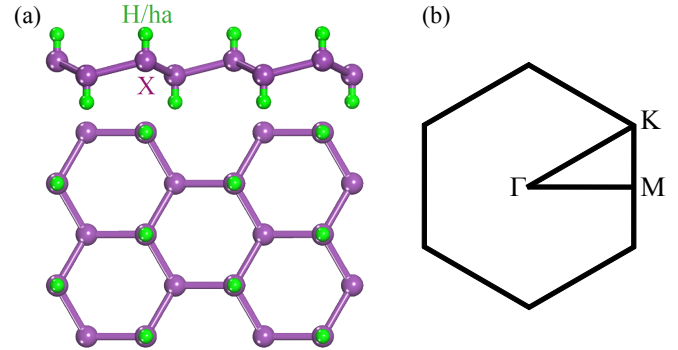


FIG. 1. (Color online). (a) The lattice geometry for 2D X -hydride/halide ($X = \text{N-Bi}$) monolayer from the side view (top) and top view (bottom). Note that two sets of sublattice in the honeycomb group V element X are not coplanar (a buckled structure). The monolayer is alternatively hydrogenated or halogenated from both sides. (b) The first Brillouin zone of 2D X -hydride/halide monolayer and the points of high symmetry.

symmetry. The concept of QSH effect was first proposed by Kane and Mele in graphene in which SOC opens a nontrivial band gap at the Dirac points.^{11,12} Subsequent works, however, showed that the SOC for graphene is tiny, hence the effect is difficult to be detected experimentally.¹³⁻¹⁵ So far, QSH effect has only been demonstrated in HgTe/CdTe quantum wells,^{16,17} and experimental evidence for helical edge modes has been presented for inverted InAs-GaSb quantum wells.¹⁸⁻²⁰ Nevertheless, these existing systems more or less have serious limitations like toxicity, difficulty in processing, and small bulk gap opened by SOC. Therefore, an easy and envi-

ronmental friendly realization of a QSH insulator is much desired. Extensive effort has been devoted to the search for new QSH insulators with large SOC gap.^{21–28} For instance, new layered honeycomb lattice type materials such as silicene, germanene²⁴ or stanene²⁵, and chemically modified stanene²⁷ have been proposed. Ultrathin Bi(111) films have drawn attention as a candidate QSH insulator, whose 2D topological properties have been reported.²⁹ An approach to design a large-gap QSH state on a semiconductor surface by a substrate orbital filtering process was also proposed.³⁰ However, desirable QSH insulators preferably with huge bulk gaps are still rare. A sizable bulk band gap in QSH insulators is essential for realizing many exotic phenomena and for fabricating new quantum devices that can operate at room temperature.

Using FP method, we have recently demonstrated that the QSH effect can be realized in the 2D hydrogenated and halogenated group-V honeycomb monolayers family, with a huge gap opened at the Dirac points due to SOC.⁵ Although the low-energy spectrum of these materials is similar to the 2D group-IV honeycomb monolayers such as graphene and silicene, the low-energy Hilbert space changes from the p_z orbital to orbitals mainly consisting of p_x and p_y from the group-V atoms (N-Bi). Moreover, the nature of the effective SOC differs between the two systems. Motivated by the fundamental interest associated with the QSH effect and huge SOC gaps in these novel 2D materials, we develop a low-energy effective model Hamiltonian that captures their essential physics. In addition, we propose a minimal four-band lattice Hamiltonian with the on-site SOC term using only the p_x and p_y orbitals.

From the symmetry analysis, the next-nearest-neighbor (NNN) intrinsic Rashba SOC should exist in these systems due to the low-buckled structure, similar to the case of silicene.²⁵ However, as we shall see, the dominant effect is from the much larger first-order SOC of on-site origin. Therefore, in the following discussion, we shall focus on the first-order on-site SOC and neglect the higher-order effects. This point will be further discussed later in this paper.

The paper is organized as follows. In Sec. II, we derive step by step the low-energy effective Hilbert subspace and Hamiltonian for honeycomb X -hydride ($X = \text{N-Bi}$) monolayers, and also investigate in detail the effective SOC. Section III presents the derivation of the low-energy effective model for X -halide ($X = \text{N-Bi}$, halide=F-I) honeycomb monolayers. In Sec. IV, a simple spinful lattice Hamiltonian for the honeycomb X -hydride/halide monolayers family is constructed. We conclude in Sec. V with a brief discussion of the effective SOC and present a summary of our results.

II. LOW-ENERGY EFFECTIVE HAMILTONIAN FOR HONEYCOMB $X\text{H}$ ($X = \text{N-Bi}$) MONOLAYERS

A. Low-energy Hilbert subspace and effective Hamiltonian without SOC

As is shown in Fig. 1(a), there are two distinct sites A and B in the unit cell of X -hydride ($X = \text{N-Bi}$) honeycomb lattice with full hydrogenation from both sides of the 2D X honeycomb sheet. The primitive lattice vectors are chosen as $\vec{a}_1 = a(1/2, \sqrt{3}/2)$ and $\vec{a}_2 = a(-1/2, \sqrt{3}/2)$, where a is the lattice constant. We consider the outer shell orbitals of textitX ($X = \text{N-Bi}$), namely s , p_x , p_y , p_z , and also the s orbital of H in the modeling. Therefore, in the representation $\{|p_y^A\rangle, |p_x^A\rangle, |p_z^A\rangle, |s_H^A\rangle, |s^A\rangle, |p_y^B\rangle, |p_x^B\rangle, |p_z^B\rangle, |s_H^B\rangle, |s^B\rangle\}$ (for simplicity, the Dirac ket symbol is omitted in the following), the Hamiltonian (without SOC) at K point with the nearest-neighbor hopping considered in the Slater-Koster formalism³¹ reads

$$H_0 = \begin{pmatrix} H_0^{AA} & H_0^{AB} \\ H_0^{AB\dagger} & H_0^{BB} \end{pmatrix}, \quad (1)$$

with

$$H_0^{AA} = \begin{bmatrix} 0 & 0 & 0 & 0 & 0 \\ 0 & 0 & 0 & 0 & 0 \\ 0 & 0 & 0 & -V_{sp\sigma}^H & 0 \\ 0 & 0 & -V_{sp\sigma}^H & \Delta_H & V_{ss\sigma}^H \\ 0 & 0 & 0 & V_{ss\sigma}^H & \Delta \end{bmatrix}, \quad (2)$$

$$H_0^{AB} = \begin{bmatrix} -V_1' & -iV_1' & 0 & 0 & V_2' \\ -iV_1' & V_1' & 0 & 0 & -iV_2' \\ 0 & 0 & 0 & 0 & 0 \\ 0 & 0 & 0 & 0 & 0 \\ -V_2' & iV_2' & 0 & 0 & 0 \end{bmatrix}, \quad (3)$$

$$H_0^{BB} = \begin{bmatrix} 0 & 0 & 0 & 0 & 0 \\ 0 & 0 & 0 & 0 & 0 \\ 0 & 0 & 0 & V_{sp\sigma}^H & 0 \\ 0 & 0 & V_{sp\sigma}^H & \Delta_H & V_{ss\sigma}^H \\ 0 & 0 & 0 & V_{ss\sigma}^H & \Delta \end{bmatrix}, \quad (4)$$

where $V_{sp\sigma}^H$ ($V_{ss\sigma}^H$) is the hopping between the p_z (s) orbital from X atom and the s orbital from H, and $V_1' \equiv (3/4)(V_{pp\pi} - V_{pp\sigma})$ and $V_2' \equiv (3/2)V_{sp\sigma}$ with $V_{pp\pi}$, $V_{sp\sigma}$, and $V_{pp\sigma}$ being the standard Slater-Koster hopping parameters. Δ and Δ_H are on-site energies for s orbitals of atom X and of atom H, respectively. The on-site energies for p orbitals are taken to be zero.

To diagonalize the Hamiltonian, we first perform the

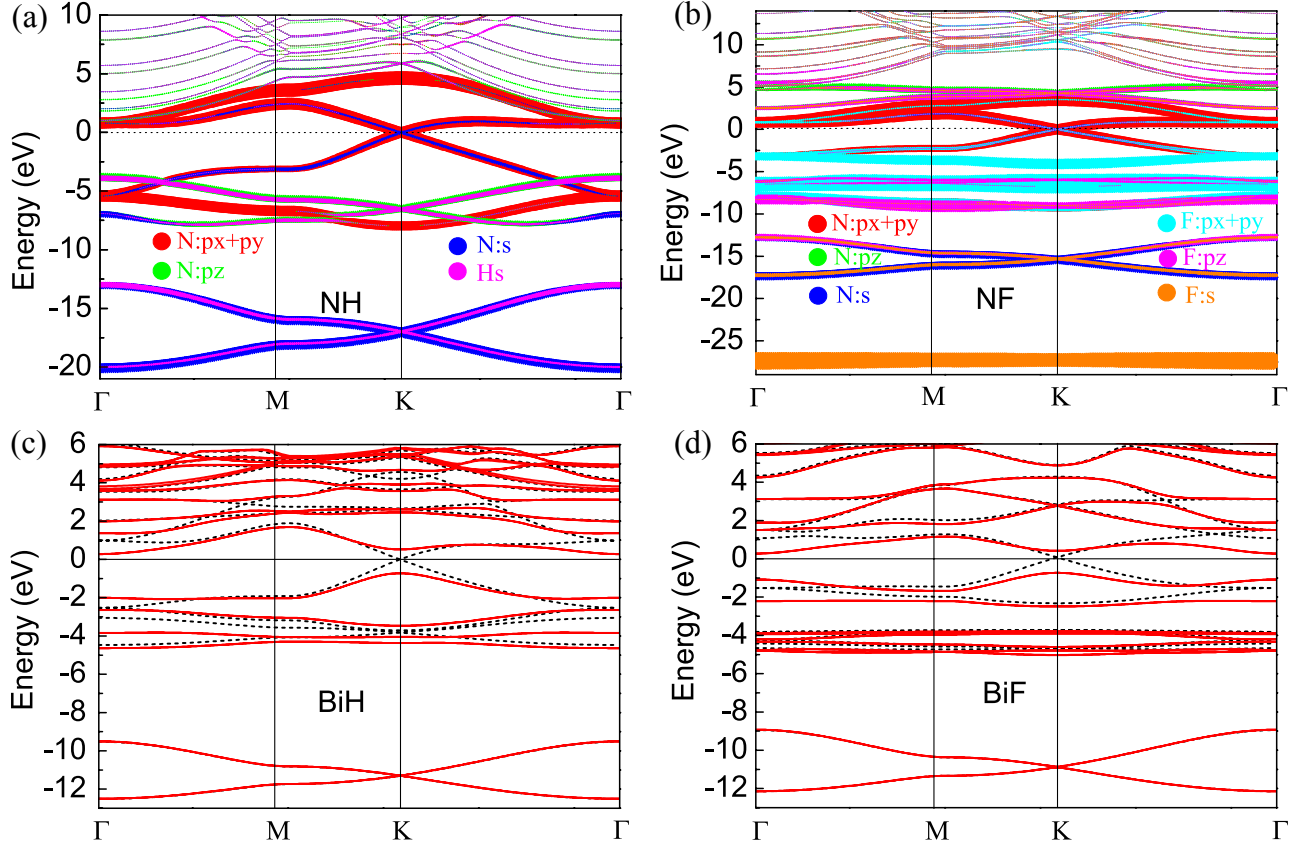


FIG. 2. (Color online). (a)(b) The partial band structure projection for NH and NF without SOC, respectively. Symbol size is proportional to the population in the corresponding states. The Fermi level is indicated by the dotted line. (c)(d) Band structures for BiH and BiF without (black dash lines) and with (red solid lines) SOC. The four band structures are obtained from the first-principles methods implemented in the VASP package³² using projector augmented wave pseudo-potential, and the exchange-correlation is treated by PAW-GGA. The Fermi level is indicated by the solid line.

following unitary transformation:

$$\begin{aligned}
 \varphi_1^A &= -\frac{1}{\sqrt{2}} (p_x^A + ip_y^A) = |p_+^A\rangle, \\
 \varphi_2^B &= \frac{1}{\sqrt{2}} (p_x^B - ip_y^B) = |p_-^B\rangle, \\
 \varphi_3 &= \frac{1}{\sqrt{2}} \left[-\frac{1}{\sqrt{2}} (p_x^A - ip_y^A) - \frac{1}{\sqrt{2}} (p_x^B + ip_y^B) \right], \\
 \varphi_4 &= \frac{1}{\sqrt{2}} \left[\frac{1}{\sqrt{2}} (p_x^A - ip_y^A) - \frac{1}{\sqrt{2}} (p_x^B + ip_y^B) \right].
 \end{aligned} \tag{5}$$

In the basis $\{\varphi_1^A, s^B, s_H^B, p_z^B, \varphi_2^B, s^A, s_H^A, p_z^A, \varphi_3, \varphi_4\}$, the Hamiltonian can be written as a block-diagonal form with three decoupled blocks H_α , H_β , and H_γ :

$$H_0 \longrightarrow H_1 = U_1^\dagger H_0 U_1, \tag{6}$$

$$U_1 = \begin{bmatrix} \frac{-i}{\sqrt{2}} & 0 & \frac{i}{2} & \frac{-i}{2} & 0 & 0 & 0 & 0 & 0 & 0 \\ \frac{-1}{\sqrt{2}} & 0 & \frac{-1}{2} & \frac{1}{2} & 0 & 0 & 0 & 0 & 0 & 0 \\ 0 & 0 & 0 & 0 & 1 & 0 & 0 & 0 & 0 & 0 \\ 0 & 0 & 0 & 0 & 0 & 1 & 0 & 0 & 0 & 0 \\ 0 & 0 & 0 & 0 & 0 & 0 & 1 & 0 & 0 & 0 \\ 0 & \frac{-i}{\sqrt{2}} & \frac{i}{2} & \frac{-i}{2} & 0 & 0 & 0 & 0 & 0 & 0 \\ 0 & \frac{1}{\sqrt{2}} & \frac{-1}{2} & \frac{1}{2} & 0 & 0 & 0 & 0 & 0 & 0 \\ 0 & 0 & 0 & 0 & 0 & 0 & 0 & 1 & 0 & 0 \\ 0 & 0 & 0 & 0 & 0 & 0 & 0 & 0 & 1 & 0 \\ 0 & 0 & 0 & 0 & 0 & 0 & 0 & 0 & 0 & 1 \end{bmatrix}, \tag{7}$$

$$H_1 = H_\alpha \oplus H_\beta \oplus H_\gamma, \tag{8}$$

with

$$H_\alpha = \begin{bmatrix} 0 & iV_2 & 0 & 0 \\ -iV_2 & \Delta & V_{ss\sigma}^H & 0 \\ 0 & V_{ss\sigma}^H & \Delta_H & V_{sp\sigma}^H \\ 0 & 0 & V_{sp\sigma}^H & 0 \end{bmatrix}, \tag{9}$$

$$H_\beta = \begin{bmatrix} 0 & -iV_2 & 0 & 0 \\ iV_2 & \Delta & V_{ss\sigma}^H & 0 \\ 0 & V_{ss\sigma}^H & \Delta_H & -V_{sp\sigma}^H \\ 0 & 0 & -V_{sp\sigma}^H & 0 \end{bmatrix}, \quad (10)$$

$$H_\gamma = \text{diag}\{V_1, -V_1\}, \quad (11)$$

where $V_1 = 2V_1'$ and $V_2 = \sqrt{2}V_2'$.

The eigenvectors for the first diagonal block H_α can be easily obtained as

$$|\varepsilon_i\rangle = \frac{1}{N_i} \begin{bmatrix} 1 \\ -i\frac{\varepsilon_i}{V_2} \\ -i\frac{\varepsilon_i^2 - \Delta\varepsilon_i - V_2^2}{V_2V_{ss\sigma}^H} \\ -i\frac{V_{sp\sigma}^H}{\varepsilon_i} \frac{\varepsilon_i^2 - \Delta\varepsilon_i - V_2^2}{V_2V_{ss\sigma}^H} \end{bmatrix}, \quad (12)$$

where ε_i and N_i ($i = 1, 2, 3, 4$) are the corresponding eigenvalues and normalization factors, respectively. Therefore, upon performing the unitary transformation $\{\phi_1, \phi_2, \phi_3, \phi_4\} = \{\varphi_1^A, s^B, s_H^B, p_z^B\}U_\alpha$ with $U_\alpha = \{|\varepsilon_i\rangle\}_{i=1,2,3,4} \equiv \{u_{ji}^\alpha\}$, the above upper-left 4×4 block H_α is diagonalized.

For the second diagonal block H_β , its eigenvalues are denoted as ε_{4+i} ($i = 1, 2, 3, 4$), and it can be easily shown that $\varepsilon_{4+i} = \varepsilon_i$, where ε_i are eigenvalues of H_α . This is consistent with FP results, i.e., there are four two-fold degeneracy points at K point as shown in Fig. 2(a). The eigenvectors of H_β are given by

$$|\varepsilon_i\rangle = \frac{1}{N_i} \begin{bmatrix} 1 \\ i\frac{\varepsilon_i}{V_2} \\ i\frac{\varepsilon_i^2 - \Delta\varepsilon_i - V_2^2}{V_2V_{ss\sigma}^H} \\ -i\frac{V_{sp\sigma}^H}{\varepsilon_i} \frac{\varepsilon_i^2 - \Delta\varepsilon_i - V_2^2}{V_2V_{ss\sigma}^H} \end{bmatrix}, \quad (13)$$

where ε_i and N_i ($i = 5, 6, 7, 8$) are the corresponding eigenvalues and normalization factors. Similar to the case of H_α , upon performing the unitary transformation $\{\phi_5, \phi_6, \phi_7, \phi_8\} = \{\varphi_2^B, s^A, s_H^A, p_z^A\}U_\beta$ with $U_\beta = \{|\varepsilon_{i+4}\rangle\}_{i=1,2,3,4} \equiv \{u_{ji}^\beta\}$, the block H_β is diagonalized.

The third block H_γ is already diagonal with eigenvalues $\{V_1, -V_1\}$ and eigenvectors $\{\phi_3, \phi_4\} \equiv \{\phi_9, \phi_{10}\}$. Therefore, in the new basis $\{\phi_1, \phi_2, \phi_3, \phi_4, \phi_5, \phi_6, \phi_7, \phi_8, \phi_9, \phi_{10}\} \equiv \{\varphi_1^A, s^B, s_H^B, p_z^B, \varphi_2^A, s^A, s_H^A, p_z^A, \varphi_3, \varphi_4\}U_2$, where $U_2 \equiv u^\alpha \oplus u^\beta \oplus I_{2 \times 2}$, the total Hamiltonian (1) takes a fully diagonalized form. The whole diagonalization process can be summarized as follows:

$$\begin{aligned} & \{\phi_1, \phi_2, \phi_3, \phi_4, \phi_5, \phi_6, \phi_7, \phi_8, \phi_9, \phi_{10}\} \\ &= \{p_y^A, p_x^A, p_z^A, s_H^A, s^A, p_y^B, p_x^B, p_z^B, s_H^B, s^B\}U, \end{aligned} \quad (14)$$

where

$$U = U_1 U_2, \quad (15)$$

$$H_0 \longrightarrow H'_0 = U^\dagger H_0 U, \quad (16)$$

$$H'_0 = \text{diag}\{\varepsilon_1, \varepsilon_2, \varepsilon_3, \varepsilon_4, \varepsilon_5, \varepsilon_6, \varepsilon_7, \varepsilon_8, V_1, -V_1\}. \quad (17)$$

From the band components projection as shown in Fig. 2(a), in the vicinity of the Dirac points (around Fermi level), the main components of the band come from the p_x and p_y orbitals of group-V element textitX mixed with a small amount of s orbital of textitX. Compared with the expressions of the eigenstates obtained above, we find that the orbital features agree with that of $|\varepsilon_1\rangle$ and $|\varepsilon_5\rangle$ if we take their eigenenergies as the Fermi energy. Therefore the corresponding states ϕ_1 and ϕ_5 constitute the low-energy Hilbert subspace. In the following, we will give the explicit forms of the low-energy states ϕ_1 and ϕ_5 as well as their eigenvalues.

Note that, in the above 4×4 H_α , the scale of the 2×2 non-diagonal block $H_{\alpha 12}$ is smaller than the difference of the typical eigenvalues between the upper 2×2 diagonal block $H_{\alpha 11}$ and the lower 2×2 diagonal block $H_{\alpha 22}$. Hence, through the downfolding procedure³³, we could obtain the low-energy effective Hamiltonian as

$$H_{\alpha 11}^{\text{eff}} = H_{\alpha 11} + H_{\alpha 12}(\varepsilon - H_{\alpha 22})^{-1}H_{\alpha 21}. \quad (18)$$

Up to the second order, one obtains

$$\varepsilon_1 = \frac{1}{2} \left(\Delta' + \sqrt{\Delta'^2 + 4V_2'^2} \right), \quad (19)$$

with

$$\begin{aligned} \Delta' &= \Delta + \frac{\varepsilon V_{ss\sigma}^{H\ 2}}{\varepsilon^2 - \Delta_H \varepsilon - V_{sp\sigma}^{H\ 2}}, \\ \varepsilon &= \frac{1}{2} \left(\Delta + \sqrt{\Delta^2 + 4V_2^2} \right). \end{aligned} \quad (20)$$

Consequently, we can obtain the explicit expressions of $|\varepsilon_1\rangle \equiv \{u_{j1}^\alpha\}_{j=1,4}$ and ϕ_1 . In a similar way, the explicit expressions of $|\varepsilon_5\rangle \equiv \{u_{j1}^\beta\}_{j=1,4}$ and ϕ_5 can also be obtained. So far, we have obtained the eigenvalues $\varepsilon_1 = \varepsilon_5$ [Eqs. (19) and (20)] and the corresponding low-energy Hilbert subspace consisting of ϕ_1 and ϕ_5 ,

$$\begin{aligned} \phi_1 &= u_{11}^\alpha \varphi_1^A + u_{21}^\alpha s^B + u_{31}^\alpha s_H^B + u_{41}^\alpha p_z^B, \\ \phi_5 &= u_{11}^\alpha \varphi_2^B - u_{21}^\alpha s^A - u_{31}^\alpha s_H^A + u_{41}^\alpha p_z^A. \end{aligned} \quad (21)$$

The above coefficients $\{u_{j1}^\alpha\}_{j=1,4}$ are given in Eq. (12).

Further simplification could be made in order to capture the main physics. We can omit the second-order correction for the eigenvalues and the first-order correction for the eigenvectors, i.e., the terms $(u_{31}^\alpha s_H^B + u_{41}^\alpha p_z^B)$ for ϕ_1 and $(-u_{31}^\alpha s_H^A + u_{41}^\alpha p_z^A)$ for ϕ_5 , and only keep the zeroth-order eigenvectors and eigenvalues,

$$\begin{aligned} \phi_1 &= u_{11}^\alpha \varphi_1^A + u_{21}^\alpha s^B, \\ \phi_5 &= u_{11}^\alpha \varphi_2^B - u_{21}^\alpha s^A, \\ \varepsilon_1 = \varepsilon &= \frac{1}{2} \left(\Delta + \sqrt{\Delta^2 + 4V_2^2} \right). \end{aligned} \quad (22)$$

This approximation is justified by our FP calculations, namely in the vicinity of the Fermi level, p_x , p_y , and s orbitals overwhelmingly dominate over the s_H and p_z orbitals in the band components.

In the Hamiltonian (17), one can take the Fermi energy $E_F = \varepsilon_1 = \varepsilon_5$ as energy zero point. Hence, states ϕ_1 and ϕ_5 , which constitute the low-energy Hilbert subspace, take the following explicit forms:

$$\begin{aligned}\phi_1 &= u_{11}^\alpha \left[-\frac{1}{\sqrt{2}} (p_x^A + ip_y^A) \right] + u_{21}^\alpha s^B, \\ \phi_5 &= u_{11}^\alpha \left[\frac{1}{\sqrt{2}} (p_x^B - ip_y^B) \right] - u_{21}^\alpha s^A,\end{aligned}\quad (23)$$

with

$$\begin{aligned}u_{11}^\alpha &= \frac{(-\Delta + \sqrt{\Delta^2 + 18V_{sp\sigma}^2})}{\sqrt{2\Delta^2 + 36V_{sp\sigma}^2 - 2\Delta\sqrt{\Delta^2 + 18V_{sp\sigma}^2}}}, \\ u_{21}^\alpha &= \frac{-3\sqrt{2}iV_{sp\sigma}}{\sqrt{2\Delta^2 + 36V_{sp\sigma}^2 - 2\Delta\sqrt{\Delta^2 + 18V_{sp\sigma}^2}}}.\end{aligned}$$

Since we are interested in the low-energy physics near the Dirac point, we perform the small \vec{k} expansion around K by $\vec{k} \rightarrow \vec{k} + K$ and keep the terms that are first order in \vec{k} . We find that

$$H_K = \begin{pmatrix} 0 & v_F k_- \\ v_F k_+ & 0 \end{pmatrix}, \quad (24)$$

with v_F being the Fermi velocity

$$v_F = \frac{\sqrt{3}a}{2} \left[\frac{1}{2} |u_{11}^\alpha|^2 (V_{pp\sigma} - V_{pp\pi}) + |u_{21}^\alpha|^2 V_{ss\sigma} \right], \quad (25)$$

and

$$k_\pm = k_x \pm ik_y.$$

Either following similar procedures, or using the inversion symmetry (or time-reversal symmetry) of the system, we can easily obtain the low-energy Hilbert subspace and the low-energy effective Hamiltonian around the K' point. Finally, we can summarize the basis for the low-energy Hilbert subspace as

$$\begin{aligned}\phi_1 &= u_{11}^\alpha \left[-\frac{1}{\sqrt{2}} (p_x^A + i\tau_z p_y^A) \right] + u_{21}^\alpha \tau_z s^B, \\ \phi_5 &= u_{11}^\alpha \left[\frac{1}{\sqrt{2}} (p_x^B - i\tau_z p_y^B) \right] - u_{21}^\alpha \tau_z s^A,\end{aligned}\quad (26)$$

and the low-energy effective Hamiltonian without SOC reads

$$H_\tau = v_F (k_x \sigma_x + \tau_z k_y \sigma_y), \quad (27)$$

where Pauli matrices σ denote the orbital basis degree of freedom, and $\tau_z = \pm 1$ labels the two valleys K and K' . Note that under the space inversion operation $P = \sigma_x \tau_x$ and the time-reversal operation $T = \tau_x \hat{K}$ (\hat{K} is the complex conjugation operator), the above low-energy effective Hamiltonian [Eq. (27)] is invariant.

B. Low-energy effective Hamiltonian involving SOC

The SOC can be written as

$$H_{so} = \xi_0 \hat{L} \cdot \hat{s} = \frac{\xi_0}{2} \left(\frac{L_+ s_- + L_- s_+}{2} + L_z s_z \right), \quad (28)$$

where $s_\pm = s_x \pm is_y$ and $L_\pm = L_x \pm iL_y$ denote the ladder operators for the spin and orbital angular momenta, respectively. Here $\hat{s} = (\hbar/2)\vec{s}$, and in the following we shall take $\hbar = 1$. ξ_0 is the magnitude of atomic SOC. Because of the presence of p_x and p_y orbital component in the low-energy Hilbert subspace [Eq. (26)] $\{\phi_1, \phi_5\} \otimes \{\uparrow, \downarrow\}$, an on-site effective SOC is generated with

$$H_{so} = \lambda_{so} \tau_z \sigma_z s_z, \quad (29)$$

where

$$\begin{aligned}\lambda_{so} &= \frac{1}{2} |u_{11}^\alpha|^2 \xi_0 \\ &= \frac{1}{2} \left[1 - \frac{9V_{sp\sigma}^2}{\Delta^2 - \Delta\sqrt{\Delta^2 + 18V_{sp\sigma}^2} + 18V_{sp\sigma}^2} \right] \xi_0.\end{aligned}\quad (30)$$

Again we stress that in the honeycomb textitX-hydride monolayers the dominant intrinsic effective SOC is on-site rather than from the NNN hopping processes as in the original Kane-Mele model.

Consequently, from the above Hamiltonian (27) and (29), we obtain the generic low-energy effective Hamiltonian around the Dirac points acting on the low-energy Hilbert subspace:

$$H_{\text{eff}} = H_\tau + H_{so} = v_F (k_x \sigma_x + \tau_z k_y \sigma_y) + \lambda_{so} \tau_z \sigma_z s_z, \quad (31)$$

where the analytical expressions for Fermi velocity v_F and magnitude of intrinsic effective SOC λ_{so} are given in Eqs. (25) and (30), whose explicit values are presented in Table I via FP calculations. Again we note that the above spinful low-energy effective Hamiltonian is invariant under both the space-inversion symmetry operation and time-reversal symmetry operation with $T = is_y \tau_x \hat{K}$.

The two model parameters v_F and λ_{so} can be obtained by fitting the band dispersions of the FP results. Their values are listed in Table I.

III. LOW-ENERGY EFFECTIVE HAMILTONIAN FOR HONEYCOMB TEXTITX-HALIDE ($X = \text{N-Bi}$) MONOLAYERS

A. Low-energy Hilbert subspace and effective Hamiltonian without SOC

For the textitX-halide ($X = \text{N-Bi}$) systems, the outer shell orbitals of X labeled as Xs , Xp_x , Xp_y , Xp_z , and the

TABLE I. Values of Fermi velocity v_F and magnitude of intrinsic SOC λ_{so} for textitX-hydride honeycomb monolayers obtained from FP calculations. Note that $\lambda_{so} = E_g/2$, with E_g the gap opened by SOC at the Dirac point.

system	v_F ($10^5 m/s$)	λ_{so} (eV)
NH	6.8	6.7×10^{-3}
PH	8.3	18×10^{-3}
AsH	8.7	97×10^{-3}
SbH	8.6	0.21
BiH	8.9	0.62

outer shell orbitals of halogen labeled as HS , Hp_x , Hp_y , Hp_z with (H=F-I) are taken into account in the following derivation. As is shown in Fig. 1(a), there are also two distinct sites A and B in the honeycomb lattice unit cell of textitX-halide with full halogenation from both sides of the 2D textitX honeycomb sheet. In the representation $\{Xp_y^A, Xp_x^A, Xp_z^A, Hp_z^A, Hp_y^A, Hp_x^A, HS^A, Xs^A, Xp_y^B, Xp_x^B, Xp_z^B, Hp_z^B, Hp_y^B, Hp_x^B, HS^B, Xs^B\}$ and at the K point, the total Hamiltonian with the nearest-neighbor hopping considered in the Slater-Koster formalism reads

$$H_0^{ha} = \begin{pmatrix} h_0^{AA} & h_0^{AB} \\ h_0^{AB\dagger} & h_0^{BB} \end{pmatrix}, \quad (32)$$

with

$$h_0^{AA} = \begin{bmatrix} 0 & 0 & 0 & 0 & V_{pp\pi}^{ha} & 0 & 0 & 0 \\ 0 & 0 & 0 & 0 & 0 & V_{pp\pi}^{ha} & 0 & 0 \\ 0 & 0 & 0 & V_{pp\sigma}^{ha} & 0 & 0 & -V_{sp\sigma}^{ha} & 0 \\ 0 & 0 & V_{pp\sigma}^{ha} & \Delta_p^{ha} & 0 & 0 & 0 & V_{sp\sigma}^{ha} \\ V_{pp\pi}^{ha} & 0 & 0 & 0 & \Delta_p^{ha} & 0 & 0 & 0 \\ 0 & V_{pp\pi}^{ha} & 0 & 0 & 0 & \Delta_p^{ha} & 0 & 0 \\ 0 & 0 & -V_{sp\sigma}^{ha} & 0 & 0 & 0 & \Delta_s^{ha} & V_{ss\sigma}^{ha} \\ 0 & 0 & 0 & V_{sp\sigma}^{ha} & 0 & 0 & V_{ss\sigma}^{ha} & \Delta \end{bmatrix}, \quad (33)$$

$$h_0^{AB} = \begin{bmatrix} -V_1' & -iV_1' & 0 & 0 & 0 & 0 & 0 & V_2' \\ -iV_1' & V_1' & 0 & 0 & 0 & 0 & 0 & -iV_2' \\ 0 & 0 & 0 & 0 & 0 & 0 & 0 & 0 \\ 0 & 0 & 0 & 0 & 0 & 0 & 0 & 0 \\ 0 & 0 & 0 & 0 & 0 & 0 & 0 & 0 \\ 0 & 0 & 0 & 0 & 0 & 0 & 0 & 0 \\ 0 & 0 & 0 & 0 & 0 & 0 & 0 & 0 \\ -V_2' & iV_2' & 0 & 0 & 0 & 0 & 0 & 0 \end{bmatrix}, \quad (34)$$

$$h_0^{BB} = \begin{bmatrix} 0 & 0 & 0 & 0 & V_{pp\pi}^{ha} & 0 & 0 & 0 \\ 0 & 0 & 0 & 0 & 0 & V_{pp\pi}^{ha} & 0 & 0 \\ 0 & 0 & 0 & V_{pp\sigma}^{ha} & 0 & 0 & V_{sp\sigma}^{ha} & 0 \\ 0 & 0 & V_{pp\sigma}^{ha} & \Delta_p^{ha} & 0 & 0 & 0 & -V_{sp\sigma}^{ha} \\ V_{pp\pi}^{ha} & 0 & 0 & 0 & \Delta_p^{ha} & 0 & 0 & 0 \\ 0 & V_{pp\pi}^{ha} & 0 & 0 & 0 & \Delta_p^{ha} & 0 & 0 \\ 0 & 0 & V_{sp\sigma}^{ha} & 0 & 0 & 0 & \Delta_s^{ha} & V_{ss\sigma}^{ha} \\ 0 & 0 & 0 & -V_{sp\sigma}^{ha} & 0 & 0 & V_{ss\sigma}^{ha} & \Delta \end{bmatrix}, \quad (35)$$

where Δ_p^{ha} is the on site energy for the p orbitals of the halogen atom, Δ_s^{ha} is the on site energy for the s orbital of textitX (halogen) atom, the on site energies for p orbitals of textitX atoms are taken to be zero. $V_{pp\pi}^{ha}$ ($V_{pp\sigma}^{ha}$) is the hopping between the p_z orbital from textitX atom and the p_z orbital from halogen atom in the "shoulder by shoulder" ("head to tail") type. $V_{sp\sigma}^{ha}$ is the hopping between the p_z (s) orbital from textitX atom and the s (p_z) orbital from halogen atom. $V_{ss\sigma}^{ha}$ is the hopping between the s orbital from textitX atom and the s orbital from halogen atom. The parameters V_1' and V_2' take the same expressions as in Sec.II A.

Firstly, we perform the unitary transformation as in Eq. (5), as well as the following unitary transformation

$$\begin{aligned} H\varphi_1^A &= -\frac{1}{\sqrt{2}} (Hp_x^A + iHp_y^A) \\ H\varphi_2^B &= \frac{1}{\sqrt{2}} (Hp_x^B - iHp_y^B) \\ H\varphi_3^A &= -\frac{1}{\sqrt{2}} (Hp_x^A - iHp_y^A) \\ H\varphi_4^B &= -\frac{1}{\sqrt{2}} (Hp_x^B + iHp_y^B) \end{aligned} \quad (36)$$

In the new basis $\{X\varphi_1^A, Xs^B, H\varphi_1^A, HS^B, Xp_z^B, Hp_z^B, X\varphi_2^B, Xs^A, H\varphi_2^B, HS^A, Xp_z^A, Hp_z^A, X\varphi_3^A, X\varphi_4^B, H\varphi_3^A, H\varphi_4^B\} = \{Xp_y^A, Xp_x^A, Xp_z^A, Hp_z^A, Hp_y^A, Hp_x^A, HS^A, Xs^A, Xp_y^B, Xp_x^B, Xp_z^B, Hp_z^B, Hp_y^B, Hp_x^B, HS^B, Xs^B\}$ U_1^{ha} , we could rewrite the Hamiltonian in the following block-diagonal form with three decoupled diagonal blocks

$$H_1^{ha} = H_{1,\alpha}^{ha} \oplus H_{1,\beta}^{ha} \oplus H_{1,\gamma}^{ha}, \quad (37)$$

$$H_{1,\alpha}^{ha} = \begin{bmatrix} 0 & iV_2 & V_{pp\pi}^{ha} & 0 & 0 & 0 \\ -iV_2 & \Delta & 0 & V_{ss\sigma}^{ha} & 0 & -V_{sp\sigma}^{ha} \\ V_{pp\pi}^{ha} & 0 & \Delta_p^{ha} & 0 & 0 & 0 \\ 0 & V_{ss\sigma}^{ha} & 0 & \Delta_s^{ha} & V_{sp\sigma}^{ha} & 0 \\ 0 & 0 & 0 & V_{sp\sigma}^{ha} & 0 & V_{pp\sigma}^{ha} \\ 0 & -V_{sp\sigma}^{ha} & 0 & 0 & V_{pp\sigma}^{ha} & \Delta_p^{ha} \end{bmatrix}, \quad (38)$$

$$H_{1,\beta}^{ha} = \begin{bmatrix} 0 & -iV_2 & V_{pp\pi}^{ha} & 0 & 0 & 0 \\ iV_2 & \Delta & 0 & V_{ss\sigma}^{ha} & 0 & V_{sp\sigma}^{ha} \\ V_{pp\pi}^{ha} & 0 & \Delta_p^{ha} & 0 & 0 & 0 \\ 0 & V_{ss\sigma}^{ha} & 0 & \Delta_s^{ha} & -V_{sp\sigma}^{ha} & 0 \\ 0 & 0 & 0 & -V_{sp\sigma}^{ha} & 0 & V_{pp\sigma}^{ha} \\ 0 & V_{sp\sigma}^{ha} & 0 & 0 & V_{pp\sigma}^{ha} & \Delta_p^{ha} \end{bmatrix}, \quad (39)$$

$$H_{1,\gamma}^{ha} = \begin{bmatrix} V_1 & 0 & \frac{V_{pp\pi}^{ha}}{\sqrt{2}} & \frac{V_{pp\pi}^{ha}}{\sqrt{2}} \\ 0 & -V_1 & -\frac{V_{pp\pi}^{ha}}{\sqrt{2}} & \frac{V_{pp\pi}^{ha}}{\sqrt{2}} \\ \frac{V_{pp\pi}^{ha}}{\sqrt{2}} & -\frac{V_{pp\pi}^{ha}}{\sqrt{2}} & \Delta_p^{ha} & 0 \\ \frac{V_{pp\pi}^{ha}}{\sqrt{2}} & \frac{V_{pp\pi}^{ha}}{\sqrt{2}} & 0 & \Delta_p^{ha} \end{bmatrix}. \quad (40)$$

For the first diagonal block $H_{1,\alpha}^{ha}$, in the presentation $\{X\varphi_1^A, Xs^B, H\varphi_1^A, Hs^B, Xp_z^B, Hp_z^B\}$ its eigenvectors can be written as

$$|\varepsilon_i^{ha}\rangle = \frac{1}{N_i^{ha}} \times \begin{bmatrix} 1 \\ \frac{i}{\sqrt{2}} \\ \frac{V_{pp\pi}^{ha}}{\sqrt{2}} \\ \frac{\varepsilon_i^{ha} - \Delta_p^{ha}}{\sqrt{2}} \\ \frac{i[V_{pp\sigma}^{ha}(V_{ss\sigma}^{ha2} + V_{pp\sigma}^{ha}V_{ss\sigma}^{ha}) - \varepsilon_i^{ha}V_{ss\sigma}^{ha}(\varepsilon_i^{ha} - \Delta_p^{ha})]}{DC} \\ \frac{-iV_{sp\sigma}^{ha}[\Delta_s^{ha}V_{pp\sigma}^{ha} - \Delta_p^{ha}V_{ss\sigma}^{ha} - \varepsilon_i^{ha}(V_{pp\sigma}^{ha} - V_{ss\sigma}^{ha})]}{DC} \\ \frac{-iV_{sp\sigma}^{ha}[V_{ss\sigma}^{ha2} + V_{ss\sigma}^{ha}V_{pp\sigma}^{ha} - \varepsilon_i^{ha}(\varepsilon_i^{ha} - \Delta_s^{ha})]}{DC} \end{bmatrix}, \quad (41)$$

with

$$D(\varepsilon_i^{ha}) \equiv (\varepsilon_i^{ha} - \Delta_s^{ha}) [V_{pp\sigma}^{ha2} - \varepsilon_i^{ha}(\varepsilon_i^{ha} - \Delta_p^{ha})] + (\varepsilon_i^{ha} - \Delta_p^{ha}) V_{sp\sigma}^{ha2}, \quad (42)$$

and

$$C \equiv \frac{V_2(\varepsilon_i^{ha} - \Delta_p^{ha})}{V_{pp\pi}^{ha2} - \varepsilon_i^{ha}(\varepsilon_i^{ha} - \Delta_p^{ha})}. \quad (43)$$

Here, ε_i^{ha} and N_i^{ha} ($i = 1, 2, \dots, 6$) are the corresponding eigenvalues and the normalization factors, respectively. Therefore, by the unitary transformation

$$\begin{aligned} & \{\phi_1^{ha}, \phi_2^{ha}, \phi_3^{ha}, \phi_4^{ha}, \phi_5^{ha}, \phi_6^{ha}\} \\ &= \{X\varphi_1^A, Xs^B, H\varphi_1^A, Hs^B, Xp_z^B, Hp_z^B\} U_\alpha, \end{aligned} \quad (44)$$

with $U_\alpha = \{|\varepsilon_i^{ha}\rangle\}_{i=1,2,\dots,6} \equiv \{u_{ji}^\alpha\}$, the above 6×6 block $H_{1,\alpha}^{ha}$ is diagonalized.

From our FP calculations [Fig. 2(b)], the main components of the band around the Dirac points and the Fermi level come from the Xp_x and Xp_y orbitals, mixed with a small amount of the Hp_x and Hp_y orbitals as well as Xs orbital. The orbital features are identical with the eigenvectors of ε_1^{ha} . When we take its eigenvalue as the

Fermi energy E_F . Following similar procedures as in the previous section, we can obtain the eigenvalues up to the second-order correction and the eigenvectors up to the first-order correction with

$$\varepsilon_1^{ha} = \frac{1}{2} \left(\Delta' + \sqrt{\Delta'^2 + 4V_2^2 - 2\frac{\Delta'V_{pp\pi}^{ha2}}{\varepsilon - \Delta_p^{ha}} + \frac{V_{pp\pi}^{ha4}}{(\varepsilon - \Delta_p^{ha})^2}} \right), \quad (45)$$

where

$$\begin{aligned} \Delta' &= \Delta - \\ & \frac{\varepsilon_1^{ha02}(V_{ss\sigma}^{ha2} + V_{sp\sigma}^{ha2}) - \varepsilon_1^{ha0}(\Delta_p^{ha}V_{ss\sigma}^{ha2} + \Delta_s^{ha}V_{sp\sigma}^{ha2})}{D(\varepsilon_i^{ha0})} + \\ & + \frac{(V_{sp\sigma}^{ha2} + V_{ss\sigma}^{ha}V_{pp\sigma}^{ha})}{D(\varepsilon_i^{ha0})}, \end{aligned} \quad (46)$$

$$\varepsilon_1^{ha0} = \frac{1}{2} \left(\Delta + \sqrt{\Delta^2 + 4V_2^2 - 2\frac{\Delta V_{pp\pi}^{ha2}}{\varepsilon - \Delta_p^{ha}} + \frac{V_{pp\pi}^{ha4}}{(\varepsilon - \Delta_p^{ha})^2}} \right), \quad (47)$$

and

$$\varepsilon = \frac{1}{2} \left(\Delta + \sqrt{\Delta^2 + 4V_2^2} \right). \quad (48)$$

Up to this point, we have found the low-energy eigenvalue ε_1^{ha} and the corresponding basis ϕ_1^{ha} . Again, in order to capture the essential physics, we simply the above expressions by taking only the zeroth-order terms. So in the following, we take $\varepsilon_1^{ha} = \varepsilon_1^{ha0}$ and omit the correction with $\{Hs^B, Xp_z^B, Hp_z^B\}$ for the eigenvector $\{|\varepsilon_1^{ha}\rangle\}$. Consequently, the eigenvector has the following form in the basis $\{X\varphi_1^A, Xs^B, H\varphi_1^A\}$

$$|\varepsilon_1^{ha}\rangle = \frac{1}{n_1^{ha}} \begin{bmatrix} 1 \\ -i\frac{V_2}{\varepsilon_1^{ha0} - \Delta} \\ \frac{V_{pp\pi}^{ha}}{\varepsilon_1^{ha0} - \Delta_p^{ha}} \end{bmatrix} \equiv \begin{bmatrix} u_{11}^{ha} \\ u_{21}^{ha} \\ u_{31}^{ha} \end{bmatrix}, \quad (49)$$

with n_1^{ha} being a normalization constant, and the eigenvalue ε_1^{ha0} is given in Eqs. (47) and (48).

The eigenvalues of the second diagonal block $H_{1,\beta}^{ha}$ are denoted as ε_{6+i}^{ha} ($i = 1, 2, \dots, 6$), and one finds that $\varepsilon_{6+i}^{ha} = \varepsilon_i^{ha}$ ($i = 1, 2, \dots, 6$), where ε_i^{ha} are eigenvalues of $H_{1,\alpha}^{ha}$. Through similar procedures, the low-energy eigenvector $\{|\varepsilon_7^{ha}\rangle\}$ has the following simple form in the basis $\{X\varphi_2^B, Xs^A, H\varphi_2^B\}$:

$$|\varepsilon_7^{ha}\rangle = \frac{1}{n_1^{ha}} \begin{bmatrix} 1 \\ i\frac{V_2}{\varepsilon_1^{ha0} - \Delta} \\ \frac{V_{pp\pi}^{ha}}{\varepsilon_1^{ha0} - \Delta_p^{ha}} \end{bmatrix} = \begin{bmatrix} u_{11}^{ha} \\ -u_{21}^{ha} \\ u_{31}^{ha} \end{bmatrix}. \quad (50)$$

The third diagonal block $H_{1,\gamma}^{ha}$ are of high energy hence is not of interest here.

From the above analysis, the low-energy states ϕ_1^{ha} and ϕ_7^{ha} constitute the low-energy Hilbert subspace. They have the following explicit forms:

$$\begin{aligned}\phi_1^{ha} &= u_{11}^{ha} \left[-\frac{1}{\sqrt{2}} (Xp_x^A + iXp_y^A) \right] + u_{21}^{ha} Xs^B \\ &\quad + u_{31}^{ha} \left[-\frac{1}{\sqrt{2}} (Hp_x^A + iHp_y^A) \right], \\ \phi_7^{ha} &= u_{11}^{ha} \left[\frac{1}{\sqrt{2}} (Xp_x^B - iXp_y^B) \right] - u_{21}^{ha} Xs^A \\ &\quad + u_{31}^{ha} \left[\frac{1}{\sqrt{2}} (Hp_x^B - iHp_y^B) \right].\end{aligned}\quad (51)$$

Again we perform the small \vec{k} expansion in the above low-energy Hilbert subspace around K point by $\vec{k} \rightarrow \vec{k} + K$ and keep the first-order terms in \vec{k} ,

$$H_K = \begin{pmatrix} 0 & v_F k_- \\ v_F k_+ & 0 \end{pmatrix}, \quad (52)$$

with v_F the Fermi velocity

$$v_F = \frac{\sqrt{3}a}{2} \left[\frac{1}{2} |u_{11}^{ha}|^2 (V_{pp\sigma} - V_{pp\pi}) + |u_{21}^{ha}|^2 V_{ss\sigma} \right]. \quad (53)$$

Note that for the textitX-halide systems, $|u_{11}^{ha}|^2$ is much larger than $|u_{21}^{ha}|^2$ and $|u_{31}^{ha}|^2$. Either following similar procedures, or via the inversion symmetry (or time-reversal symmetry), one can obtain the low-energy Hilbert subspace and the low-energy effective Hamiltonian around the K' point. Finally the basis for low-energy Hilbert subspace can be summarized as

$$\begin{aligned}\phi_1^{ha} &= u_{11}^{ha} \left[-\frac{1}{\sqrt{2}} (Xp_x^A + i\tau_z Xp_y^A) \right] + u_{21}^{ha} \tau_z Xs^B \\ &\quad + u_{31}^{ha} \left[-\frac{1}{\sqrt{2}} (Hp_x^A + i\tau_z Hp_y^A) \right], \\ \phi_7^{ha} &= u_{11}^{ha} \left[\frac{1}{\sqrt{2}} (Xp_x^B - i\tau_z Xp_y^B) \right] - u_{21}^{ha} \tau_z Xs^A \\ &\quad + u_{31}^{ha} \left[\frac{1}{\sqrt{2}} (Hp_x^B - i\tau_z Hp_y^B) \right].\end{aligned}\quad (54)$$

and the low-energy effective Hamiltonian without SOC reads

$$H_\tau = v_F (k_x \sigma_x + \tau_z k_y \sigma_y), \quad (55)$$

where Pauli matrices σ denote the orbital basis degree of freedom, and τ_z labels the two valleys K and K' . Note that under the space reversal operation $P = \sigma_x \tau_x$ and the time-reversal operation $T = \tau_x \hat{K}$, the above low-energy effective Hamiltonian Eq. (55) is also invariant.

B. Low-energy effective Hamiltonian involving SOC

In a similar way as in Sec. II B, we obtain an on-site SOC in the spinful low-energy Hilbert subspace $\{\phi_1, \phi_7\} \otimes \{\uparrow, \downarrow\}$,

$$H_{so} = \lambda_{so} \tau_z \sigma_z s_z, \quad (56)$$

$$\lambda_{so} = \frac{1}{2} |u_{11}^{ha}|^2 \xi_0^X + \frac{1}{2} |u_{31}^{ha}|^2 \xi_0^{ha}, \quad (57)$$

where u_{11}^{ha} and u_{31}^{ha} are given in Eq. (49), and ξ_0^X (ξ_0^{ha}) is the magnitude of atomic SOC of pnictogen (halogen). It should be noted that due to the presence of major p_x and p_y orbital components, the first-order on-site effective SOC also dominates in the textitX-halide systems. Equation (49) explains the tendency that the λ_{so} increases with the atomic number of halogen for the same pnictogen element, as shown in Table II.

From Eqs. (55) and (56), we obtain the generic low-energy effective Hamiltonian around the Dirac points acting on the low-energy Hilbert subspace $\{\phi_1, \phi_7\} \otimes \{\uparrow, \downarrow\}$

$$H_{\text{eff}} = H_\tau + H_{so} = v_F (k_x \sigma_x + \tau_z k_y \sigma_y) + \lambda_{so} \tau_z \sigma_z s_z, \quad (58)$$

where Fermi velocity v_F and magnitude of intrinsic effective SOC λ_{so} are given in Eqs. (53) and (57), and their values are listed in Table II. One notes that this Hamiltonian is also invariant under both the space-inversion symmetry and time-reversal symmetry with $T = i s_y \tau_x \hat{K}$.

The two model parameters v_F and λ_{so} for halides obtained by fitting the band dispersions of the FP results are listed in Table II.

IV. A SIMPLE SPINFUL LATTICE HAMILTONIAN FOR THE HONEYCOMB TEXTITX-HYDRIDE/HALIDE ($X = \text{N-BI}$) MONOLAYERS FAMILY

For the purpose of studying the topological properties of the honeycomb textitX-hydride/halide ($X = \text{N-Bi}$) monolayers family, as well as their edge states, it is convenient to work with a lattice Hamiltonian via lattice regularization of the low-energy continuum models (Eq. (31) and Eq. (58)). Taking into account the main physics involving p_x and p_y orbitals, we construct the following spinful lattice Hamiltonian for the 2D honeycomb textitX-hydride/halide ($X = \text{N-Bi}$) monolayers

$$\begin{aligned}H &= \sum_{\langle i,j \rangle; \alpha, \beta = p_x, p_y} t_{ij}^{\alpha\beta} c_{i\alpha}^\dagger c_{j\beta} \\ &\quad + \sum_{i; \alpha, \beta = p_x, p_y; \sigma, \sigma' = \uparrow, \downarrow} \lambda_{\sigma, \sigma'}^{\alpha\beta} c_{i\alpha\sigma}^\dagger c_{i\beta\sigma'} s_{\sigma, \sigma'}^z,\end{aligned}\quad (59)$$

where $\langle i, j \rangle$ means i and j sites are nearest neighbors, α and β are the orbital indices. The first term is the hopping term and the second one is the on-site SOC term.

TABLE II. Values of two model parameters v_F and λ_{so} for honeycomb textitX-halide ($X = \text{N-Bi}$) monolayers obtained from FP calculations. Note that $\lambda_{so} = E_g/2$, with E_g the gap opened by SOC at the Dirac point.

system	v_F (10^5 m/s)	λ_{so} (eV)	system	v_F (10^5 m/s)	λ_{so} (eV)
NF	5.5	8.5×10^{-3}	NBr	4.2	19×10^{-3}
PF	7.2	13×10^{-3}	PBr	8.0	17×10^{-3}
AsF	7.3	80×10^{-3}	AsBr	8.2	98×10^{-3}
SbF	6.6	0.16	SbBr	7.7	0.20
BiF	7.2	0.55	BiBr	7.3	0.65
NCl	4.3	9.7×10^{-3}	NI	3.8	28×10^{-3}
PCl	7.8	17×10^{-3}	PI	8.1	19×10^{-3}
AsCl	8.0	95×10^{-3}	AsI	9.1	0.10
SbCl	7.3	0.19	SbI	7.7	0.21
BiCl	6.9	0.56	BiI	7.7	0.65

After Fourier transformation of the above lattice Hamiltonian, its energy spectrum over the entire Brillouin zone can be obtained. Since here spin is good quantum number, we can divide the model Hamiltonian into two sectors for spin up and spin down separately. For each sector, the corresponding model Hamiltonian reads

$$H^\uparrow(k) = \begin{bmatrix} 0 & -\frac{i\xi_0}{2} & h_{xx}^{AB}(k) & h_{xy}^{AB}(k) \\ 0 & h_{xy}^{AB}(k) & h_{yy}^{AB}(k) & 0 \\ \dagger & 0 & -\frac{i\xi_0}{2} & 0 \end{bmatrix}, \quad (60)$$

$$H^\downarrow(k) = \begin{bmatrix} 0 & \frac{i\xi_0}{2} & h_{xx}^{AB}(k) & h_{xy}^{AB}(k) \\ 0 & h_{xy}^{AB}(k) & h_{yy}^{AB}(k) & 0 \\ \dagger & 0 & \frac{i\xi_0}{2} & 0 \end{bmatrix}, \quad (61)$$

where

$$h_{xx}^{AB}(k) \equiv \frac{1}{2} (3V_{pp\sigma} + V_{pp\pi}) \cos\left(\frac{k_x}{2}\right) \exp\left(i\frac{k_y}{2\sqrt{3}}\right) + V_{pp\pi} \exp\left(-i\frac{k_y}{\sqrt{3}}\right),$$

$$h_{xy}^{AB}(k) \equiv i\frac{\sqrt{3}}{2} (V_{pp\sigma} - V_{pp\pi}) \sin\left(\frac{k_x}{2}\right) \exp\left(i\frac{k_y}{2\sqrt{3}}\right),$$

and

$$h_{yy}^{AB}(k) \equiv \frac{1}{2} (V_{pp\sigma} + 3V_{pp\pi}) \cos\left(\frac{k_x}{2}\right) \exp\left(i\frac{k_y}{2\sqrt{3}}\right) + V_{pp\sigma} \exp\left(-i\frac{k_y}{\sqrt{3}}\right).$$

For simplicity, we choose the lattice constant $a = 1$. The on-site energies for p orbitals are taken to be zero. Near the K and K' points, the above model Hamiltonian reduces to the low-energy effective Hamiltonian [Eq. (31) and (58)] with $v_F = \frac{\sqrt{3}a}{4} (V_{pp\sigma} - V_{pp\pi})$ and $\lambda_{so} = \xi_0/2$.

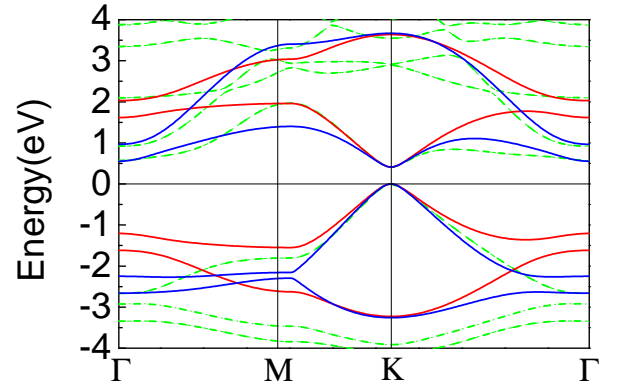


FIG. 3. (Color online). A comparison of the band structures for monolayer SbH calculated using FP and TB methods with SOC. The dashed green curve is the FP result. The solid red and blue curves are the TB model results. The red curve is with the NN hopping only, while the blue curve also includes the NNN hopping terms. For the NN case, the parameters are taken as $V_{pp\sigma} = 1.68 \text{ eV}$, $V_{pp\pi} = -0.60 \text{ eV}$. For the NNN case, the parameters are taken as $V_{pp\sigma} = 1.69 \text{ eV}$, $V_{pp\pi} = -0.62 \text{ eV}$, $V_{pp\sigma}^{NNN} = 0 \text{ eV}$, $V_{pp\pi}^{NNN} = -0.23 \text{ eV}$. For both cases, $\lambda_{so} = 0.21 \text{ eV}$. The superscript NNN means the next-nearest-neighbor hopping. The Fermi level is set to zero.

Taking SbH as an example, we compare the results from FP calculations and from the lattice models. As shown in Fig. 3, there is a good agreement between the two results around the K point. The fitting away from K point can be improved by including hopping terms between far neighbors. In Fig. 3, we also show the result with NNN hopping, for which a fairly good agreement with the FP low-energy bands over the whole Brillouin zone can be achieved.

V. DISCUSSION AND SUMMARY

We have obtained the low-energy effective Hamiltonian for the textitX-hydride and textitX-halide ($X = \text{N-Bi}$) family of materials, which is analogous to the Kane-Mele model proposed for the QSH effect in graphene.¹¹ The important difference is that in Kane-Mele model the effective SOC is of second-order NNN type, which is much weaker than the on-site SOC in our systems. The SOC term in our Hamiltonian opens a large nontrivial gap at the Dirac points. From K to K' the mass term changes sign for each spin species and the band is inverted. As a result, the QSH effect can be realized in the textitX-hydride and textitX-halide ($X = \text{N-Bi}$) monolayers. Some of these materials, such as BiH/BiF, have record huge SOC gap with magnitude around 1 eV, far higher than the room-temperature energy scale, hence making their detection much easier.

On the experimental side, the buckling honeycomb Bi(111) monolayer and film have been manufactured via molecular beam epitaxy (MBE).^{23,29,34} On the other hand, chemical functionalization of 2D materials is a powerful tool to create new materials with desirable features, such as modifying graphene into graphane, graphone, and fluorinated graphene via H and F, respectively.³⁵ Therefore, it is very promising that Bi-Hydride/Halide monolayer, the huge gap QSH insulators, may be synthesized by chemical reaction in the solvents or by the exposure of the Bi (111) monolayer and film to the atomic or molecular gases. It is noted that even though one side (full passivation) instead of both sides (alternating passivation) of Bi(111) bilayers is passivated, the band structure is almost unchanged and the topology properties remain nontrivial. This will provide more freedom to realize these kinds of materials.

It is known that the low-energy Hilbert space for graphene consists of the p_z orbital from carbon atoms. In that system, the SOC term from NNN second-order processes is vanishingly small, and the on-site SOC as well as the nearest neighbor SOC are forbidden by symmetry constraint. In contrast, for the honeycomb textitX-hydride/halide monolayers, p_x and p_y orbitals from the group V elements constitute the low-energy Hilbert subspace. In fact, this represents the first class of materials for which the Dirac fermion physics is associated with p_x and p_y orbitals. Because of this, the effective on-site SOC can have nonzero matrix elements and results in the huge SOC gap at the Dirac points.

The leading-order effective SOC processes in the textitX-hydride and textitX-halide systems, silicene, and graphene are schematically shown in Fig. 4. As shown in Figs. 4(a) and 4(b), the representative leading-order effective SOC processes around the K point in the honeycomb textitX-hydride and textitX-halide monolayers are

$$\begin{aligned} |p_{+\uparrow}^A\rangle &\xrightarrow{\lambda_{so}} |p_{+\uparrow}^A\rangle, & |p_{+\downarrow}^A\rangle &\xrightarrow{-\lambda_{so}} |p_{+\downarrow}^A\rangle, \\ |p_{-\uparrow}^B\rangle &\xrightarrow{-\lambda_{so}} |p_{-\uparrow}^B\rangle, & |p_{-\downarrow}^B\rangle &\xrightarrow{\lambda_{so}} |p_{-\downarrow}^B\rangle, \end{aligned} \quad (62)$$

where λ_{so} represents the atomic spin-orbit interaction strength, which is given in Eq. (30) for textitX-hydride systems and Eq. (57) for textitX-halide systems. In a Hilbert subspace consisting of p_x and p_y orbitals, such effective SOC arises in the first-order on-site processes, which leads to its huge magnitude.

As for silicene, which has a low-buckled structure, the typical leading-order SOC is from the (first-order) NNN processes,²⁵ as shown in Fig. 4(c),

$$\begin{aligned} |p_{z\uparrow}^A\rangle &\xrightarrow{V} |p_{-\uparrow}^B\rangle \xrightarrow{-\frac{\xi_0}{2}} |p_{-\uparrow}^B\rangle \xrightarrow{V} |p_{z\uparrow}^A\rangle, \\ |p_{z\downarrow}^A\rangle &\xrightarrow{V} |p_{-\downarrow}^B\rangle \xrightarrow{\frac{\xi_0}{2}} |p_{-\downarrow}^B\rangle \xrightarrow{V} |p_{z\downarrow}^A\rangle, \\ |p_{z\uparrow}^B\rangle &\xrightarrow{V} |p_{+\uparrow}^A\rangle \xrightarrow{-\frac{\xi_0}{2}} |p_{+\uparrow}^A\rangle \xrightarrow{V} |p_{z\uparrow}^B\rangle, \\ |p_{z\downarrow}^B\rangle &\xrightarrow{V} |p_{+\downarrow}^A\rangle \xrightarrow{\frac{\xi_0}{2}} |p_{+\downarrow}^A\rangle \xrightarrow{V} |p_{z\downarrow}^B\rangle, \end{aligned} \quad (63)$$

where V is the nearest-neighbor direct hopping amplitude and ξ_0 represents the atomic intrinsic SOC strength. The whole process can be divided into three steps. For example, we consider the p_z^A orbital. Firstly, due to the low-buckled structure, p_z^A couples to p_-^B . Carriers in p_z^A orbital then hop to the nearest neighbor p_-^B orbital. Secondly, the atomic intrinsic SOC shifts the energy of the spin up and spin down carriers by $\mp \frac{\xi_0}{2}$. In the third step, carriers in the p_-^B orbital hop to another nearest-neighbor p_z^A orbital, making the resulting effective SOC an NNN process and of first order in ξ_0 .

As for graphene, around Dirac point, the leading-order effective SOC is from (second-order) NNN effective SOC process, as shown in Fig. 4(d):

$$\begin{aligned} |p_{z\uparrow}^A\rangle &\xrightarrow{\xi_0/\sqrt{2}} |p_{+\downarrow}^A\rangle \xrightarrow{V} |s_{\downarrow}^B\rangle \xrightarrow{V} |p_{+\downarrow}^A\rangle \xrightarrow{\xi_0/\sqrt{2}} |p_{z\uparrow}^A\rangle, \\ |p_{z\downarrow}^B\rangle &\xrightarrow{\xi_0/\sqrt{2}} |p_{-\uparrow}^B\rangle \xrightarrow{V} |s_{\uparrow}^A\rangle \xrightarrow{V} |p_{-\uparrow}^B\rangle \xrightarrow{\xi_0/\sqrt{2}} |p_{z\downarrow}^B\rangle. \end{aligned} \quad (64)$$

During the whole NNN hopping process, the atomic SOC appears twice, making the effective SOC second order in ξ_0 and hence much weaker.

In summary, using the TB method and the FP calculation, we have derived the low-energy effective Hilbert subspace and Hamiltonian for the honeycomb textitX-hydride/halide monolayers materials. These 2D group-V honeycomb lattice materials have the same low-energy effective Hamiltonian due to their same D_{3d} point group symmetry and the same D_3 small group at the K and K' points. The low-energy model contains two key parameters v_F and λ_{so} . We have obtained their analytic expressions and also their numerical values by fitting the FP calculations. Moreover, we have found that the low-energy Hilbert subspace consists of p_x and p_y orbitals from the group-V elements, which is a key reason for the huge SOC gap. This feature is distinct from the group-IV honeycomb lattice monolayers such as silicene and graphene. Finally, we construct a spinful lattice Hamiltonian for these materials. Our results will be useful for further investigations of this intriguing class of materials.

ACKNOWLEDGMENTS

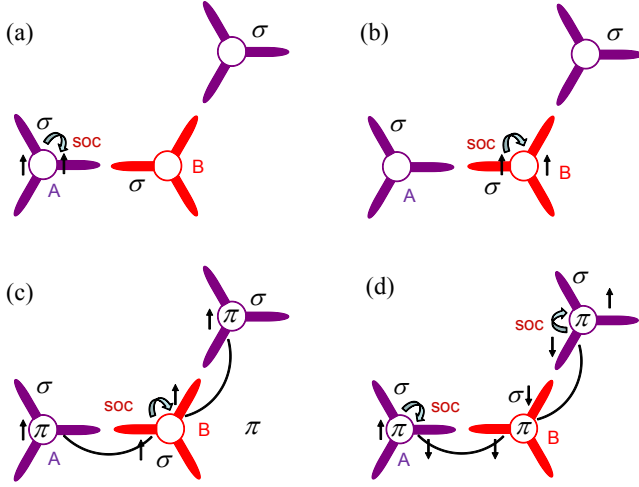


FIG. 4. (Color online). The leading-order effective SOC processes in textitX-hydride or textitX-halide ($X = \text{N-Bi}$), silicene and graphene. (a) and (b) Sketches of the huge effective on-site SOC in textitX-hydride systems and textitX-halide systems. (c) Sketch of the effective SOC from NNN hopping processes caused by the buckling in silicene. (d) Sketch of the second-order effective SOC from NNN hopping processes in graphene.

This work was supported by the MOST Project of China (Nos. 2014CB920903, 2010CB833104, and 2011CBA00100), the National Natural Science Foundation of China (Grant Nos. 11225418, 51171001, and 11174337), SUTD-SRG-EPD2013062, and the Specialized Research Fund for the Doctoral Program of Higher Education of China (Grant No. 20121101110046). Cheng-Cheng Liu was supported Excellent young scholars Research Fund of Beijing Institute of Technology (Grant No. 2014CX04028).

Note added Recently, we notice another relevant work³⁶ discussing effective models of a honeycomb lattice with p_x and p_y orbitals.

* ygyao@bit.edu.cn

- ¹ A. K. Gelm and K. S. Novoselov, Nat. Mater. **6**, 183-191 (2007).
- ² A. H. Castro Neto, F. Guinea, N. M. R. Peres, K. S. Novoselov, and A. K. Geim, Rev. Mod. Phys. **81**, 109 (2009).
- ³ P. Vogt, P. De Padova, C. Quaresima, J. Avila, E. Frantzeskakis, M. C. Asensio, A. Resta, B. Ealet, and G. Le Lay, Phys. Rev. Lett. **108**, 155501 (2012).
- ⁴ L. Chen, C.-C. Liu, B. Feng, X. He, P. Cheng, Z. Ding, S. Meng, Y. Yao, and K. Wu, Phys. Rev. Lett. **109**, 056804 (2012).
- ⁵ Z. Song, C.-C. Liu, J. Yang, J. Han, B. Fu, Y. Yang, Q. Niu, J. Lu, and Y.G. Yao, arXiv:cond-mat/1402.2399.
- ⁶ C. Wu, D. Bergman, L. Balents, and S. Das Sarma, Phys. Rev. Lett. **99**, 070401 (2007).
- ⁷ C. Wu, Phys. Rev. Lett. **100**, 200406 (2008).
- ⁸ M. Z. Hasan and C. L. Kane, Rev. Mod. Phys. **82**, 3045 (2010).
- ⁹ X. Qi and S. Zhang, Rev. Mod. Phys. **83**, 1057 (2011).
- ¹⁰ B. Yan and S.-C. Zhang, Rep. Prog. Phys. **75**, 096501 (2012).
- ¹¹ C. L. Kane and E. J. Mele, Phys. Rev. Lett. **95**, 226801 (2005).
- ¹² C. L. Kane and E. J. Mele, Phys. Rev. Lett. **95**, 146802 (2005).
- ¹³ Y. G. Yao, F. Ye, X. L. Qi, S. C. Zhang, and Z. Fang, Phys. Rev. B **75**, 041401(R) (2007).
- ¹⁴ H. Min, J. E. Hill, N. A. Sinitsyn, B. R. Sahu, L. Kleinman, and A. H. MacDonald, Phys. Rev. B **74**, 165310 (2006).
- ¹⁵ S. Konschuh, M. Gmitra, and J. Fabian, Phys. Rev. B **82**, 245412 (2010).
- ¹⁶ B. A. Bernevig, T. L. Hughes, and S. C. Zhang, Science **314**, 1757-1761 (2006).
- ¹⁷ M. König, S. Wiedmann, C. Brüne, A. Roth, H. Buhmann, L. W. Molenkamp, X. L. Qi, and S.C. Zhang, Science **318**, 766-770 (2007).
- ¹⁸ C. X. Liu, T. L. Hughes, X. L. Qi, K. Wang, and S. C. Zhang, Phys. Rev. Lett. **100**, 236601 (2008).
- ¹⁹ I. Knez, R.R. Du, and G. Sullivan, Phys. Rev. Lett. **107**, 136603 (2011).
- ²⁰ I. Knez, R.R. Du, and G. Sullivan, Phys. Rev. Lett. **109**, 186603 (2012).
- ²¹ S. Murakami, Phys. Rev. Lett. **97**, 236805 (2006).
- ²² Z. Liu, C. X. Liu, Y.S. Wu, W.H. Duan, F. Liu, and Jian Wu, Phys. Rev. Lett. **107**, 136805 (2011).
- ²³ T. Hirahara, G. Bihlmayer, Y. Sakamoto, M. Yamada, H. Miyazaki, S.I. Kimura, S. Blügel, and S. Hasegawa, Phys. Rev. Lett. **107**, 166801 (2011).
- ²⁴ C.-C. Liu, W. Feng, and Y. Yao, Phys. Rev. Lett. **107**, 076802 (2011).
- ²⁵ C.-C. Liu, H. Jiang, and Y. Yao, Phys. Rev. B **84**, 195430 (2011).
- ²⁶ C. Weeks, J. Hu, J. Alicea, M. Franz, and R. Wu, Phys. Rev. X **1**, 021001 (2011).
- ²⁷ Y. Xu, B. Yan, H.-J. Zhang, J. Wang, G. Xu, P. Tang, W. Duan, and S.-C. Zhang, Phys. Rev. Lett. **111**, 136804 (2013).
- ²⁸ Z.F. Wang, Z. Liu, and F. Liu, Nat. Commun. **4**, 1471 (2013).
- ²⁹ F. Yang, L. Miao, Z. F. Wang, M.-Y. Yao, F. Zhu, Y. R. Song, M.-X. Wang, J.-P. Xu, A. V. Fedorov, Z. Sun, G. B. Zhang, C. Liu, F. Liu, D. Qian, C. L. Gao, and J.-F. Jia, Phys. Rev. Lett. **109**, 016801 (2012).

- ³⁰ M. Zhou, W. Ming, Z. Liu, Z. Wang, Y.G. Yao, and F. Liu, arXiv:cond-mat/1401.3392.
- ³¹ J. C. Slater and G. F. Koster, Phys. Rev. **94**, 1498 (1954).
- ³² G. Kresse and J. Furthmüller, Phys. Rev. B **54**, 11169-11186 (1996).
- ³³ R. Winkler, *Spin-Orbit Coupling Effects in Two-Dimensional Electron and Hole Systems*, 1st ed. (Springer, Berlin, 2003).
- ³⁴ C. Sabater, D. Gosálbez-Martínez, J. Fernández-Rossier, J. G. Rodrigo, C. Untiedt, and J. J. Palacios, Phys. Rev. Lett. **110**, 176802 (2013).
- ³⁵ J. O. Sofo, A. S. Chaudhari, and G. D. Barber, Phys. Rev. B **75**, 153401 (2007); D. C. Elias, R. R. Nair, T. M. G. Mohiuddin, S. V. Morozov, P. Blake, M. P. Halsall, A. C. Ferrari, D. W. Boukhvalov, M. I. Katsnelson, A. K. Geim, K. S. Novoselov, Science **323**, 610 (2009); J. Zhou, Q. Wang, Q. Sun, X. S. Chen, Y. Kawazoe, and P. Jena, Nano Lett. **9**, 3867 (2009); J. T. Robinson, J. S. Burgess, C. E. Junkermeier, S. C. Badescu, T. L. Reinecke, F. K. Perkins, M. K. Zalalutdniov, J. W. Baldwin, J. C. Culbertson, P. E. Sheehan, and E. S. Snow, ibid. **10**, 3001 (2010).
- ³⁶ G.-F. Zhang, Y. Li, and C. Wu, arXiv:cond-mat/1403.0563.